crystals

MDPI

Article

$Pr_{9.33}(SiO_4)_6O_2$ Crystals: Czochralski Growth and Near UV-Visible FR Performance

Xin Chen and Jianzhong Chen *

College of Chemistry, Fuzhou University, Fuzhou 350116, China; xin.chen@fzu.edu.cn
* Correspondence: j.z.chen@fzu.edu.cn; Tel.: +86-591-22866243

Academic Editor: Shujun Zhang
Received: 29 June 2017; Accepted: 21 July 2017; Published: 31 July 2017

Abstract: $Pr_{9.33}(SiO_4)_6O_2$ crystals have been grown by the Cz-method for the first time for near UV–visible Faraday rotation applications. Rietveld refinement of XRD data demonstrates that the compound crystallizes in the oxyapatite structure with space group $P6_3/m$, with oxyapatite structure. In contrast to $Tb_3Ga_5O_{12}$, $Pr_{9.33}(SiO_4)_6O_2$ crystal shows a higher transparency in the UV–visible wavelength region, and a shorter cutoff at 270 nm. The Faraday rotation performance and the temperature-dependence of the field-cooled (FC) and zero-field-cooled (ZFC) magnetic susceptibility have been investigated, which indicate that the $Pr_{9.33}(SiO_4)_6O_2$ crystal exhibits paramagnetic behavior in the experimental temperature range from 2 to 300 K and yields a larger FR angle which rapidly increases towards the cutoff. $Pr_{9.33}(SiO_4)_6O_2$ crystal is therefore a promising magneto-optical crystal in particular for potential FR applications in the near UV–visible spectral region.

Keywords: magneto-optic material; Czochralski technique; magnetism; Faraday rotation

1. Introduction

The Faraday isolators (FIs) using the non-reciprocity principle are poised to be a significant player in a modern optical information processing system to eliminate optical noise and feedback [1–5]. Yttrium-iron garnet ($Y_3Fe_5O_{12}$, YIG), the most commonly used FI material in the near IR spectral region so far, is transparent in the 1.2~5.0 μm wavelength regions and exhibits an extremely large Faraday rotation (FR) angle [6,7]. Nevertheless, with the rapid expansion of visible solid-state lasers and laser-diodes, as well as excimer lasers in the UV, the demand of FIs operated at these spectral regions is rapidly promoting [8–10], while the conventional Yttrium-iron garnet crystals are not practical because of their poor transparency in this wavelength region [11].

The most widely employed magneto-optical (MO) materials for the visible and near IR spectral regions are terbium-gallium garnet ($Tb_3Ga_5O_{12}$, TGG) crystals [1,12] and Tb-doped glasses [13–15]. Nevertheless, due to poor relative stability and low thermal conductivity, Tb-doped glasses could not be employed in high-power lasers [16]. For another, TGG crystal, as a crystalline MO material, is a congruently melting material and therefore can be synthesized by the Czochralski (Cz) method. However, because of the evaporation and decomposition of Ga_2O_3 from the congruent melt during the Czochralski growth process, its growth technique is not exempt of difficulties [17,18]. Furthermore, owing to the electric-dipole 4*f*-4*f* transitions of the MO active ion Tb^{3+}, TGG crystal presents two physical drawbacks: the increasing transmission loss in the visible spectral region, and the strong absorption bands in the near UV [19]. Therefore, with the continuous development of fiber-lasers and laser-diodes operating at shorter spectral regions, the demand of FIs operating in the UV–visible wavelength region is rapidly increasing.

Among the rare earth ions, Tb^{3+}, Ce^{3+}, Pr^{3+}, and Dy^{3+} have been pointed to exhibit the best MO performance [20,21], and Pr^{3+} is more transparent in the near UV. Taking into account the requirements

for a new generation of MO materials employed in the near UV–visible spectral region, $Pr_{9.33}(SiO_4)_6O_2$ (PSO), a member of the oxyapatite-type silicate [22–24], which crystallizes in the hexagonal system and demonstrates great potential for application in phosphors [25] and high-power lasers [26,27], has attracted growing attention from our research team in recent years.

PSO crystal melts congruently and presents strong crystallizability [28], hence, in the present investigation, we try to adopt the common RF-heating Cz-method to grow PSO crystals. The optical transmission, magnetic, and magneto-optical performances have also been discussed.

2. Experimental

PSO single crystals were synthesized by the common Cz-technique with RF-heating [29]. The polycrystalline materials used for PSO crystals growth were synthesized by the solid-phase reaction method using high-purity initial reagents Pr_6O_{11}, and SiO_2 powders. The stoichiometric amounts of starting materials were weighed accurately with the overweight 1 wt% of SiO_2 in order to make up for its potential volatilization losses during the PSO crystals growth. The raw materials mixed homogeneously in a corundum mortar with the ethanol were pressed into tablets and then sintered at 1470 K in air for 23 h.

The polycrystalline tablets with single apatite phase were added into an iridium crucible with dimensions of Ø56 × 43 mm^2, and then heated by a ratio frequency induction furnace under a protective atmosphere of N_2. After the PSO polycrystalline material was melted completely, the <001> oriented PSO crystal, obtained through growth on the iridium wire, was used as seeds and dipped into the PSO melt with 15~20 rpm rotating rate and 1.0~1.5 mm h^{-1} pulling rate. After growth, the PSO crystal was pulled out of the melt and then annealed at a rate of 15~60 K h^{-1} to room temperature.

The photograph of the as-grown PSO single crystal is shown in Figure 1a. The PSO crystal is crack free and transparent with a light green coloration. Owing to the optically uniaxial crystal, PSO single crystal should be oriented along the crystallographic c-axis to avoid the effects of birefringence in the FR measurements. The PSO crystal was oriented by X-ray diffraction, and the wafers, cut along the (001) crystal plane, are shown in Figure 1b.

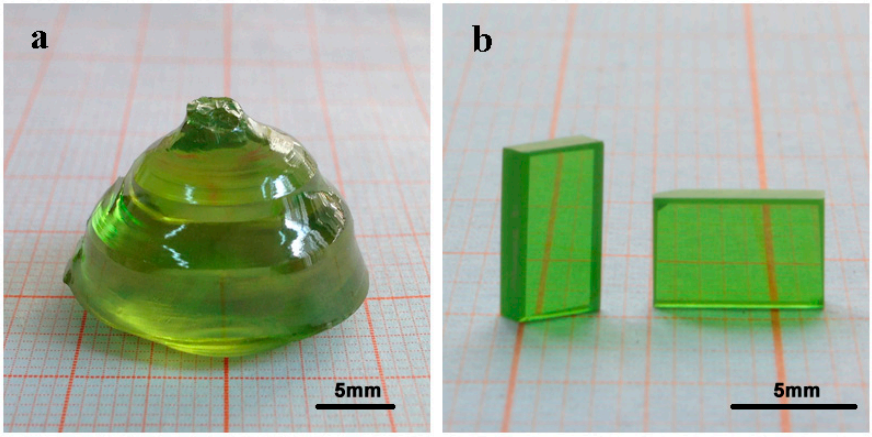

Figure 1. Photographs of as-grown PSO single crystal (**a**), and polished wafers (**b**).

The X-ray diffraction measurement for Rietveld refinement were carried out on a Rigaku-Ultima III X-ray diffractometer (Rigaku, Tokyo, Japan) using the Cu-K_α line (λ = 1.54051 Å) between $10° < 2\theta < 80°$ with a scanning step of 0.01° and a scanning rate of 0.12°/min at room temperature. Structural parameter refinement of PSO crystal was carried out by analyzing the X-ray diffraction data using the DBWS-9411 PC program [30]. The absorption spectrum of as-grown PSO crystal was tested by using a Lambda900 UV-Vis-NIR spectrophotometer (Perkin-Elmer, Waltham, MA, USA), over the spectral range of 200–800 nm at room temperature with a 2 nm resolution. The temperature-dependence

of the field-cooled (FC) and zero-field-cooled (ZFC) magnetic susceptibilities were tested by using a superconducting quantum interference device magnetometer (SQUID, Quantum Design MPMS-XL, San Diego, CA, USA) in the temperature range from 2 to 300 K with an applied field of 0.1 T. Faraday rotation angles of the as-grown PSO single crystal along the crystallographic c-axis were measured by using the photo-extinction technique [31] at room temperature with the average values of six data for interpretation. A commercial TGG single crystal, supplied by Physcience Opto-electronic Co., Ltd. Beijing, was used as a reference material and has also been evaluated under the same test conditions.

3. Results and Discussion

3.1. Structure Refinement

The powder X-ray diffraction pattern of the as-grown PSO single crystal are displayed in Figure 2. The Rietveld refinement unambiguously indicates the existence of the single hexagonal oxyapatite phase with the space group $P6_3/m$. The atomic coordinates, unit cell parameters, and refinement results for the as-grown PSO crystal are compiled in Table 1, which indicate that each cation occupies the expected cationic site according to the atomic radius, that is, $Pr_{9.33}(SiO_4)_6O_2$. The 6*h* sites are fully occupied by Pr^{3+} and the cation vacancy are all present at the 4*f* sites with concentration of 6.7%. It is noteworthy that the oxide ions coordinated by Pr (1) ions at the 4*f* site are all belong to $(SiO_4)_4$ group. However, the other oxide ions, at the 2a site, have three-fold coordination with the Pr (2) ions at the 6*h* site and do not belong to any $(SiO_4)_4$ group. Therefore, placing Pr ions on the 6*h* site can satisfy electrostatic charge balance more efficiently. On the other hand, the 4*f* site is an ionic site, while the 6*h* site is a covalent site on the basis of the bond valence sums [32]. So it seems to be that the cation vacancies are preferred at the 4*f* site. These conclusions from our Rietveld refinement present good agreement with previous ones found in other oxyapatite-type silicates [22–24,28].

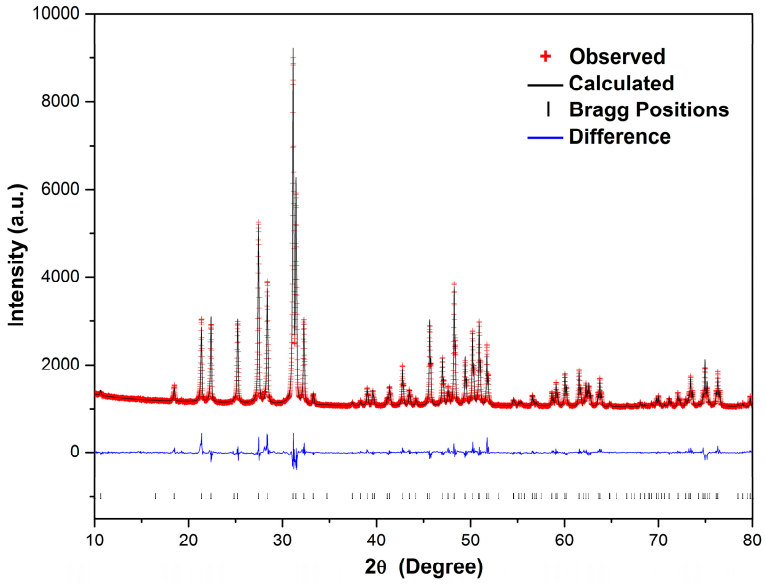

Figure 2. Fitted diffraction profiles of the as-grown PSO single crystal at room temperature.

Table 1. Refined structural parameters for the as-grown PSO crystal according to $P6_3/m$ model.

Atom	Site	Site Occ.	*x*	*y*	*z*
Pr1	4*f*	0.849	1/3	2/3	0.0014
Pr2	6*h*	1.0	0.0124	0.2400	1/4
Si	6*h*	1.0	0.3935	0.3702	1/4
O1	6*h*	1.0	0.3165	0.4693	1/4
O2	6*h*	1.0	0.5813	0.4818	1/4
O3	12i	1.0	0.3432	0.2570	0.0735
O4	2a	1.0	0	0	1/4

Hexagonal, space group $P6_3/m$; a = b = 9.61229(3) Å, c = 7.06561(2) Å, R_{wp} = 6.52%.

3.2. Optical Transmission

The absorption spectrum of as-grown crystal PSO in the near UV–visible spectral region is given in Figure 3, in contrast to the commercial TGG crystal. As can be seen, the absorbance of TGG continuously increases in the visible spectral region till the beginning of the $^7F_6 \rightarrow {}^5D_3$, $^5D_2$ Tb^{3+} absorption bands below 390 nm, which seriously restricts the application of TGG FIs in the UV–visible spectral region. In comparison with TGG, PSO crystal presents a smaller dispersion, a higher transparency in the near UV–visible spectral region, and a shorter cutoff at 265 nm, which enables the use of PSO single crystals also at spectral region where TGG crystals could not be employed. However, a strong absorption band, attributed to the energy level transition $^3H_4 \rightarrow {}^1S_0$ reduces the transparency below 270 nm. In addition, PSO presents two absorption bands in the 430–497 nm and the 570–612 nm wavelength regions, which are mainly related to the energy level transitions $^3H_4 \rightarrow {}^3P_J$ and $^3H_4 \rightarrow {}^1D_2$ of Pr^{3+} in the oxyapatite structure, and responsible for the typical light green coloration of PSO crystal.

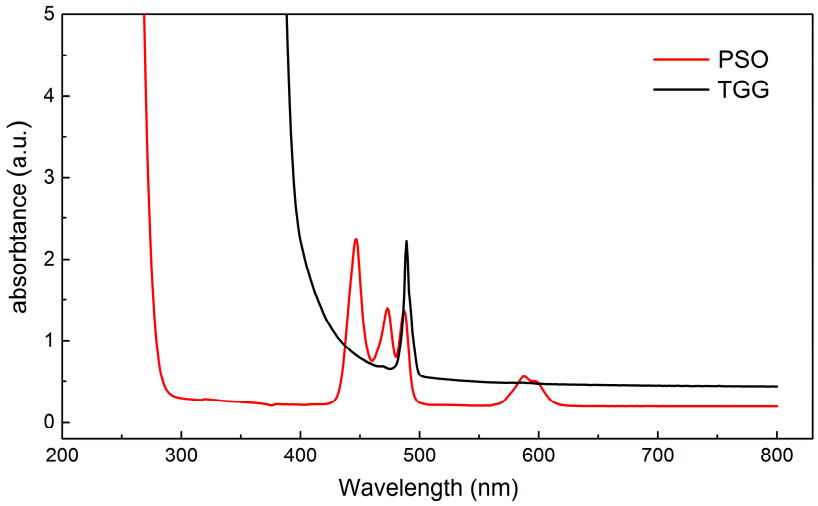

Figure 3. Absorption spectra of as-grown PSO crystal in comparison with that of commercial TGG crystal.

3.3. Paramagnetic Behavior

The temperature-dependence of the magnetic susceptibility (χ_M) for as-grown PSO crystal measured over the temperature range from 2 to 300 K are exhibited in Figure 4. Paramagnetic behavior was observed in the experimental temperature range, that is, no magnetic interaction was found down to 2.0 K. The reciprocal magnetic susceptibility as a function of the temperature is shown in the inset of Figure 4, and the solid line indicated a Curie–Weiss behavior above 70 K. The deviation from the Curie-Weiss law below 70 K may related to the influence of the crystal field on the magnetic

ions Pr^{3+} in the PSO compound [33,34]. A fit of the ${\chi_M}^{-1} - T$ curve to the Curie–Weiss law from 200 to 300 K gives the effective magnetic moment (μ_{eff}) of PSO to be 3.54(3) μ_B, which is in good agreement with the theoretical effective magnetic moment for a free Pr^{3+} ion, i.e., μ_{cal} = 3.58 μ_B [35].

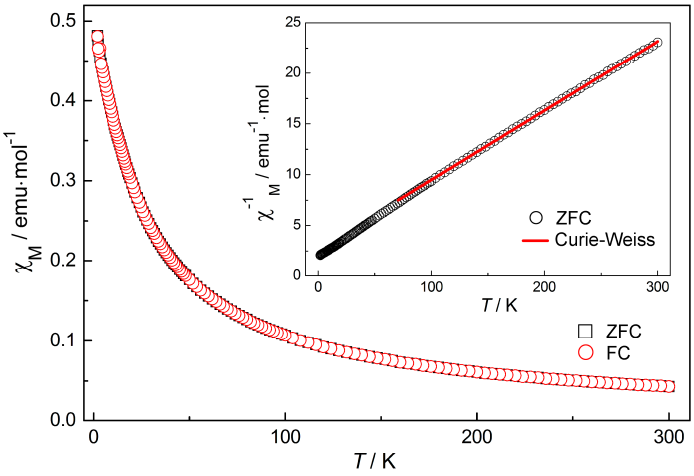

Figure 4. Temperature-dependence of the magnetic susceptibility for as-grown crystal PSO. The inset shows the reciprocal magnetic susceptibility vs. temperature curve. The solid line is the Curie–Weiss fitting.

3.4. Magneto-Optical Performance

The magneto-optical response of as-grown PSO single crystal along the crystallographic c-axis at room temperature is exhibited in Figure 5 as a function of the wavelength. It is seen that, although PSO crystal just has a slightly larger Faraday rotation angle than that of the commercial TGG crystal in the visible spectral region, the Verdet constant increment of PSO in the near UV spectral region is very remarkable: V_{PSO} varies from 511 to 1590 rad T^{-1} m^{-1} between 400 and 300 nm.

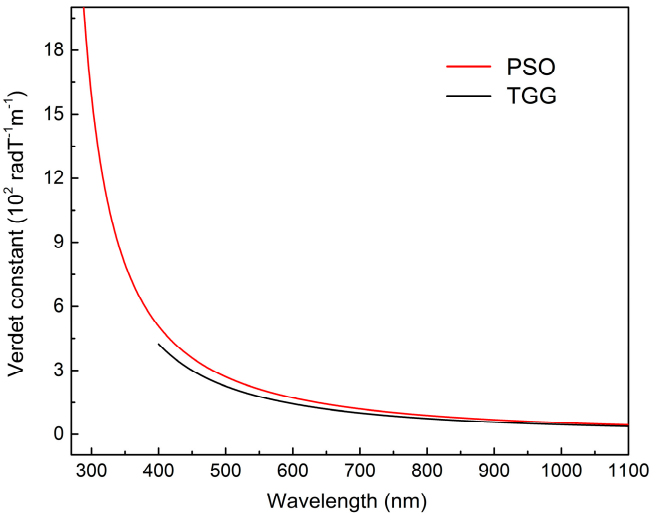

Figure 5. Verdet constant of as-grown PSO crystal vs. wavelength λ. TGG was tested as reference, and the experimental data were fitted by an equation $A/(\lambda^2 - {\lambda_0}^2)$, with λ_0 and A constants.

On the basis of FR standard theory, which considers a single electronic transition frequency, the Verdet constants (V), are proportional to the inverse of the wavelength square (λ^2) and to the concentration of magnetic rare-earth ions (N_{RE}) as follows

$$V = \frac{E}{\lambda^2 - \lambda_0^2} \quad (1)$$

where λ_0 corresponds to the wavelength of RE^{3+} ions $4f$-$4f5d$ transition, and the factor E includes all the proportionality factor, e.g., the Lande splitting factor, the concentration of magnetic ions N_{RE}, and the transition probability [36]. Fitting the experimental data to Equation (1) yields E and λ_0, listed in Table 2. As magneto-optic effect of PSO crystal comes mainly from Pr ions, we can assume that the concentration of magnetic ions and Pr ions is approximately the same. The concentration of Pr ions can be obtained according to the refined structural parameters of PSO. As shown in Table 2, the transition wavelengths of Pr^{3+} in PSO is slightly smaller than that of Tb^{3+} in TGG at 239 and 260 nm, respectively. Moreover, the rotation efficiency of Tb^{3+} in TGG clearly overcomes that of Pr^{3+} in PSO, i.e., $(E/N_{Tb})_{TGG} > (E/N_{Pr})_{PSO}$. Hence, it can be deduced that the larger Verdet constant observed in PSO is merely owing to a higher concentration of the MO active RE^{3+} ions. Moreover, in comparison with PrF_3, PSO crystal not only presents a larger transition wavelength, i.e., $(\lambda_0)_{PSO} > (\lambda_0)_{PrF3}$, but also a higher rotation efficiency, i.e., $(E/N_{Pr})_{PSO} >> (E/N_{Pr})_{PrF3}$, which makes it have a larger Verdet constant than that of PrF_3 [2].

Table 2. The fitted results of PSO, TGG, and PrF_3 single crystals according to Equation (1), and the respective RE^{3+} ion concentrations N_{RE} in the crystals.

Crystal	λ_0 (nm)	E (10^7 rad nm^2 T^{-1} m^{-1})	N_{RE} (10^{21} ions cm^{-3})
PSO	239	5.2755	16.71
TGG	260	4.2595	12.74
PrF_3 [2]	184	4.5965	19.10

4. Conclusions

In summary, the performance of oxyapatite-type PSO crystals for magneto-optical applications in the near UV–visible spectral region was investigated. Crack free PSO single crystals with high optical-quality and large size were successfully fabricated by the Cz-method. The Rietveld refinement indicates that the as-grown PSO crystallizes in $P6_3/m$, with oxyapatite structure. As expected, PSO crystal exhibits paramagnetic behavior down to 2 K and presents a higher transparency in the near UV–visible spectral region, as well as a shorter cutoff at 265 nm. In comparison with Pr-based crystal PrF_3 and commercially available TGG, we demonstrate that the as-grown PSO crystal yields a larger FR which rapidly increases towards the cutoff. Presented results therefore indicate that PSO crystals are promising magneto-optical crystal in particular for potential magneto-optical applications in the near UV–visible spectral region.

Acknowledgments: This work was supported by National Natural Science Foundation of China (Nos. 51602054, 61575045 and 51272044), and the Natural Science Foundation of Fujian Province (No. 2013J01180).

Author Contributions: Xin Chen and Jianzhong Chen conceived and designed the experiments; Xin Chen performed the experiments, analyzed the data, and wrote the paper; Jianzhong Chen modified the article.

Conflicts of Interest: The authors declare no conflict of interest.

References

1. Khazanov, E.; Andreev, N.; Palashov, O.; Poteomkin, A.; Sergeev, A.; Mehl, O.; Reitze, D.H. Effect of terbium gallium garnet crystal orientation on the isolation ratio of a Faraday isolator at high average power. *Appl. Opt.* **2002**, *41*, 483–492. [CrossRef] [PubMed]

2. Vasyliev, V.; Villora, E.G.; Nakamura, M.; Sugahara, Y.; Shimamura, K. UV–visible Faraday rotators based on rare-earth fluoride single crystals: $LiREF_4$ (RE = Tb, Dy, Ho, Er and Yb), PrF_3 and CeF_3. *Opt. Express* **2012**, *20*, 14460–14470. [CrossRef] [PubMed]
3. Bedarev, V.A.; Pashchenko, M.I.; Merenkov, D.N.; Savina, Y.O.; Pashchenko, V.O.; Gnatchenko, S.L.; Bezmaternykh, L.N.; Temerov, V.L. The Faraday effect in $TbFe_3(BO_3)_4$ and $TbAl_3(BO_3)_4$ borates. *J. Magn. Magn. Mater.* **2014**, *362*, 150–153. [CrossRef]
4. Tsushima, K.; Koshizuka, N. Research activities on magneto-optical devices in Japan. *IEEE Trans. Magn.* **1987**, *23*, 3473–3478. [CrossRef]
5. Tanaka, K.; Tatehata, N.; Fujita, K.; Hirao, K.; Soga, N. The Faraday effect and magneto-optical figure of merit in the visible region for lithium borate glasses containing Pr^{3+}. *J. Phys. D Appl. Phys.* **1998**, *31*, 2622–2627. [CrossRef]
6. Shoji, Y.; Mizumoto, T.; Yokoi, H.; Hsieh, I.W.; Osgood, R.M. Magneto-optical isolator with silicon waveguides fabricated by direct bonding. *Appl. Phys. Lett.* **2008**, *92*, 071117. [CrossRef]
7. Modi, K.B.; Vara, R.P.; Vora, H.G.; Chhantbar, M.C.; Joshi, H.H. Infrared spectroscopic study of Fe^{3+} substituted yttrium iron garnet. *J. Mater. Sci.* **2004**, *39*, 2187–2189. [CrossRef]
8. Lee, D.; Choi, K.; Kim, K.D.; Park, Y. Visible light wireless communications based on predistorted OFDM. *Opt. Commun.* **2012**, *285*, 1767–1770. [CrossRef]
9. Cui, K.Y.; Quan, J.G.; Xu, Z.Y. Performance of indoor optical femtocell by visible light communication. *Opt. Commun.* **2013**, *298–299*, 59–66. [CrossRef]
10. Das, P.; Park, Y.; Kim, K.D. Performance of color-independent OFDM visible light communication based on color space. *Opt. Commun.* **2014**, *324*, 264–268. [CrossRef]
11. Geho, M.; Sekijima, T.; Fujii, T. Growth of terbium aluminum garnet ($Tb_3Al_5O_{12}$; TAG) single crystals by the hybrid laser floating zone machine. *J. Cryst. Growth* **2004**, *267*, 188–193. [CrossRef]
12. Yasuhara, R.; Tokita, S.; Kawanaka, J.; Kawashima, T.; Kan, H.; Yagi, H.; Nozawa, H.; Yanagitani, T.; Fujimoto, Y.; Yoshida, H.; et al. Cryogenic temperature characteristics of Verdet constant on terbium gallium garnet ceramics. *Opt. Express* **2007**, *15*, 11255–11261. [CrossRef] [PubMed]
13. Giesen, A.; Speiser, J. Fifteen years of work on thin-disk lasers: Results and scaling laws. *IEEE J. Sel. Top. Quantum* **2007**, *13*, 598–609. [CrossRef]
14. Hayakawa, T.; Nogami, M.; Nishi, N.; Sawanobori, N. Faraday rotation effect of highly Tb_2O_3/Dy_2O_3-concentrated $B_2O_3-Ga_2O_3-SiO_2-P_2O_5$ glasses. *Chem. Mater.* **2002**, *14*, 3223–3225. [CrossRef]
15. Chen, Q.L.; Wang, H.; Wang, Q.W.; Chen, Q.P. Properties of tellurite core/cladding glasses for magneto-optical fibers. *J. Non-Cryst. Solids* **2014**, *400*, 51–57. [CrossRef]
16. Miyanaga, N.; Azechi, H.; Tanaka, K.A.; Kanabe, T.; Jitsuno, T.; Kawanaka, J.; Fujimoto, Y.; Kodama, R.; Shiraga, H.; Knodo, K.; et al. 10-kJ PW laser for the FIREX-I program. *J. Phys. IV France* **2006**, *133*, 81–87. [CrossRef]
17. Linares, R.C. Growth of garnet laser crystals. *Solid State Commun.* **1964**, *2*, 229–231. [CrossRef]
18. Carruthers, J.R.; Kokta, M.; Barns, R.L.; Grasso, M. Nonstoichiometry and crystal growth of gadolinium gallium garnet. *J. Cryst. Growth* **1973**, *19*, 204–208. [CrossRef]
19. Chen, X.; Zhang, W.H.; Wan, Q.P.; Guo, F.Y.; Zhuang, N.F.; Fu, H.; Xie, X.T.; Chen, J.Z. Czochralski growth of $Sr_2Tb_8(SiO_4)_6O_2$ crystals for visible–near IR magneto-optical applications. *Opt. Mater.* **2014**, *37*, 188–192. [CrossRef]
20. Berger, S.B.; Rubinstein, C.B.; Kurkjian, C.R.; Treptow, A.W. Faraday rotation of rare-earth (III) phosphate glasses. *Phys. Rev.* **1964**, *133*, A723–A727. [CrossRef]
21. MacFarlane, D.R.; Bradbury, C.R.; Newman, P.J.; Javorniczky, J. Faraday rotation in rare earth fluorozirconate glasses. *J. Non-Cryst. Solids* **1997**, *213–214*, 199–204. [CrossRef]
22. Higuchi, M.; Katase, H.; Kodaira, K.; Nakayama, S. Float zone growth and characterization of $Pr_{9.33}(SiO_4)_6O_2$ and $Sm_{9.33}(SiO_4)_6O_2$ single crystals with an apatite structure. *J. Cryst. Growth* **2000**, *218*, 282–286. [CrossRef]
23. Kolitsch, U.; Seifert, H.J.; Aldinger, F. The Identity of Monoclinic La_2O_3 and Monoclinic Pr_2O_3 With $La_{9.33}(SiO_4)_6O_2$ and $Pr_{9.33}(SiO_4)_6O_2$, Respectively. *J. Solid State Chem.* **1995**, *120*, 38–42. [CrossRef]
24. Masubuchi, Y.; Higuchi, M.; Takeda, T.; Kikkawa, S. Oxide ion conduction mechanism in $RE_{9.33}(SiO_4)_6O_2$ and $Sr_2RE_8(SiO_4)_6O_2$ (RE = La, Nd) from neutron powder diffraction. *Solid State Ion.* **2006**, *177*, 263–268. [CrossRef]

25. Yamane, A.; Kunimoto, T.; Kobayashi, H. Luminescent properties of Tb-activated rare-earth oxyapatite silicate $MLn_4Si_3O_{13}$ (M = Ca, Sr, Ln = La, Gd). *Phys. Status Solidi C* **2006**, *3*, 2705–2708. [CrossRef]
26. Lebedev, V.A.; Voroshilov, I.V.; Ignatiev, B.V.; Gavrilenko, A.N.; Isaev, V.A.; Shestakov, A.V. Spectroscopy of ytterbium in $Gd_4CaO(SiO_4)_3$ (CGS). *J. Lumin.* **2000**, *92*, 139–144. [CrossRef]
27. Druon, F.; Chénais, S.; Raybaut, P.; Balembois, F.; Georges, P.; Gaumé, R.; Haumesser, P.H.; Viana, B.; Vivien, D.; Dhellemmes, S.; et al. Apatite-structure crystal, Yb^{3+}: $SrY_4(SiO_4)_3O$, for the development of diode-pumped femtosecond lasers. *Opt. Lett.* **2002**, *27*, 1914–1916. [CrossRef]
28. Chen, X.; Gong, Z.L.; Fu, H.; Zhuang, N.F.; Zhang, W.H.; Xie, X.T.; Guo, F.Y.; Chen, J.Z. Czochralski growth and Faraday rotation properties of $Tb_{9.33}(SiO_4)_6O_2$ crystals. *J. Cryst. Growth* **2015**, *418*, 126–129. [CrossRef]
29. Liebertz, J. Crystal growth from melts of high viscosity. *Prog. Cryst. Growth Charact.* **1983**, *6*, 361–369. [CrossRef]
30. Young, R.A.; Shakthivel, A.; Moss, T.S.; Paiva-Santos, C.O. *DBWS*-9411-an upgrade of the *DBWS**.* programs for Rietveld refinement with PC and mainframe computers. *J. Appl. Crystallogr.* **1995**, *28*, 366–367. [CrossRef]
31. Yoshida, H.; Tsubakimoto, K.; Fujimoto, Y.; Mikami, K.; Fujita, H.; Miyanaga, N.; Nozawa, H.; Yagi, H.; Yanagitani, T.; Nagata, Y.; et al. Optical properties and Faraday effect of ceramicterbium gallium garnet for a room temperatureFaraday rotator. *Opt. Express* **2011**, *19*, 15181–15187. [CrossRef] [PubMed]
32. Takahashi, M.; Uematsu, K.; Ye, Z.G.; Sato, M. Single-Crystal Growth and Structure Determination of a new oxide apatite, $NaLa_9(GeO_4)_6O_2$. *J. Solid State Chem.* **1998**, *139*, 304–309. [CrossRef]
33. Rosenkranz, S.; Ramirez, A.P.; Hayashi, A.; Cava, R.J.; Siddharthan, R.; Shastry, B.S. Crystal-field interaction in the pyrochlore magnet $Ho_2Ti_2O_7$. *J. Appl. Phys.* **2000**, *87*, 5914–5916. [CrossRef]
34. Gingras, M.; Hertog, B.; Faucher, M.; Gardner, J.; Dunsiger, S.; Chang, L.; Gaulin, B.; Raju, N.; Greedanm, J. Thermodynamic and single-ion properties of Tb^{3+}within thecollective paramagnetic-spin liquid state of the frustrated pyrochlore antiferromagnet $Tb_2Ti_2O_7$. *Phys. Rev. B* **2000**, *62*, 6496–6511. [CrossRef]
35. Hiroaki, N.; Makoto, W.; Yukio, H. Crystal structures, magnetic and thermal properties of Ln_3IrO_7(Ln=Pr, Nd, Sm, and Eu). *J. Solid State Chem.* **2004**, *177*, 739–744.
36. Qiu, J.R.; Tanaka, K.; Sugimoto, N.; Hirao, K. Faraday effect in Tb^{3+}-containing borate, fluoride and fluorophosphates glasses. *J. Non-Cryst. Solids* **1997**, *213–214*, 193–198. [CrossRef]